

Pinching of ICME Flux Rope: Unprecedented Multipoint Observations of Internal Magnetic Reconnection during Gannon's Superstorm

SHIBOTOSH BISWAS,¹ ANKUSH BHASKAR,¹ ANIL RAGHAV,² AJAY KUMAR,² KALPESH GHAG,² SMITHA V. THAMPI,¹ AND VIPIN K YADAV¹

¹Space Physics Laboratory, Vikram Sarabhai Space Centre, Indian Space Research Organization, Trivandrum, Kerala 695022, India*

²Department of Physics, University of Mumbai, Vidyanagari, Santacruz (E), Mumbai 400098, India

ABSTRACT

The extreme solar storm of May 10, 2024, during the 25th solar cycle, which recorded a symmetric H component index (Sym-H) reaching -500 nT, was the strongest since the 2003 Halloween storm. This event offered a unique opportunity for unprecedented multipoint observation of the complex interaction of Interplanetary Coronal Mass Ejections (ICME) from different vantage points. Utilizing NASA's Wind, ACE, DSCOVR, THEMIS-C, STEREO-A, MMS, and ISRO's recently launched Aditya-L1 spacecraft, we comprehensively investigated the spatio-temporal variations in interplanetary plasma and magnetic field parameters. Our study reveals large-scale quasi-steady magnetic reconnection within the interior of the ICME flux rope, possibly triggered by interactions between multiple ICMEs. A current sheet (CS) forms within the flux rope, enabling internal magnetic reconnection between concentric magnetic surfaces, which leads to a sharp reversal of the IMF B_y component, as observed at the L1 point. Concurrently, reconnection exhaust and enhanced electron and ion fluxes were detected with the CS, extending over 200 R_E (1.3 million km) along the GSE-y direction. This finding sheds new light on the role of internal reconnection in ICME evolution, highlighting its pivotal role in modifying the morphology of the ICME magnetic structure and exerting severe space weather effects on Earth.

Keywords: Magnetic reconnection, Geomagnetic storm, ICME, Magnetic cloud, Solar wind

1. INTRODUCTION

In our increasingly technology-dependent world, extreme space weather has emerged as a critical concern. Solar eruptions, particularly coronal mass ejections (CMEs), modulate the heliospheric plasma and are the primary drivers of severe space weather events (Kilpua et al. 2017), disrupting satellite operations, communication networks, GPS systems, and power grids, posing substantial risks to infrastructure and human activities (Hapgood 2017; Hayakawa et al. 2020). A crucial challenge in space weather prediction is accurately determining the arrival time of interplanetary CMEs (ICMEs) at the Earth (Riley et al. 2018), but equally important is understanding their magnetic topology. The orientation and internal structure of an ICME magnetic field critically influence solar Wind-magnetosphere energy transfer, affecting the severity of geomagnetic storms (Teng et al. 2024; Gonzalez et al. 2011). Thus, precise predictions of both the ICME arrival and morphology are vital for mitigating the impact of space weather.

One such extreme solar and geomagnetic storm occurred from May 10 to 12, 2024, known as Gannon's or Mother's Day Storm. The Earth's magnetopause (a boundary between solar and magnetospheric plasma) was compressed below 5 Earth radii (1 R_E = 6371 km) (Fu et al. 2025), exposing geostationary satellites to harsh solar wind conditions. Although geomagnetic disturbances on Earth are primarily driven by the southward component of the interplanetary magnetic field (IMF- B_z) (Gonzalez et al. 1994; Ashna et al. 2024), studies have established the critical impact of IMF- B_y also (Holappa et al. 2020, 2021; Chakrabarty et al. 2017). A sudden change in the IMF- B_y and IMF- B_z orientation alters the coupling between solar wind and magnetosphere. These transient events affect the efficiency of energy transfer from the solar wind to the ionosphere through the magnetosphere (Vichare & Bagiya 2024; Ohtani

* Department of Physics, University of Kerala, Trivandrum, India

et al. 2025; Zhang et al. 2025; Venugopal et al. 2025), which modulates auroral and even low-latitude ionospheric activities significantly. However, the underlying cause of this drastic change in IMF orientation and morphology remained unclear, prompting a detailed investigation into its origin.

Multiple CMEs from the Sun arriving on May 10 & 11 were responsible for the intense geomagnetic storm observed on Earth (Kwak et al. 2024). CMEs are plasma bursts with magnetic fields that release an enormous amount of energy into interplanetary space from the solar corona (Gosling et al. 1974; St. Cyr et al. 2000). The first ICME observations in the 1970s revealed loop- or bubble-like structures associated with closed magnetic fields, often described as magnetic flux ropes (MFRs) (Hirshberg et al. 1970; Gosling et al. 1973; Palmer et al. 1978). The trajectory of the observing spacecraft decides the inferred structure of the ICME. If the observation displays: (1) enhanced magnetic field compared to surroundings ($> 10 nT$); (2) smooth rotation of magnetic field components over a large angle; and (3) reduced proton temperature and plasma beta (ratio between thermal and magnetic pressure of plasma) (Kilpua et al. 2017; Klein & Burlaga 1982), the ICME can be classified as a Magnetic Cloud (MC) (Burlaga et al. 1981). ICME flux ropes might have high plasma beta; however, only those flux ropes with the above properties are denominated magnetic clouds. These ICMEs generate a shock ahead of them due to their relatively higher speed compared to the communication speed in the solar wind. The region between the shock front and the MC is filled with a turbulent and compressed plasma medium with a fluctuating magnetic field, high plasma density, and temperature, known as the ICME sheath. Comprehensive reviews of ICMEs and their solar-terrestrial interactions are available in the literature (Gopalswamy 2016; Kilpua et al. 2017; Webb & Howard 2012).

ICMEs undergo dynamic transformations, such as twisting, pinching, kinking, and magnetic reconnection, throughout their evolution, from initiation to propagation, while interacting with the ambient solar wind (Manchester IV et al. (2005); Niembro et al. (2019); Pal et al. (2020); Wang et al. (2016) and references therein) and significantly alters their morphology, often flattening them into a ‘Pancake’ (Manchester IV et al. 2004; Raghav et al. 2019). For example, twisting magnetic field lines can cause kinking and pinching within the MC, potentially fragmenting it into multiple large-scale plasmoids (Khabarova et al. 2015, 2016). Within these compressed flux ropes, reconnection is expected to occur frequently due to variations in magnetic field orientations (Khabarova et al. 2021). In short, magnetic reconnection is a fundamental plasma process in the universe in which magnetic energy is efficiently converted into kinetic energy, heat, and particle acceleration (Gonzalez & Parker 2016) and could play a significant role in ICME evolution in the heliosphere.

A considerable number of studies have been conducted to date for this extreme solar event of May 2024 from its origin, propagation, and effect on geospace (Kruparova et al. 2024; Kwak et al. 2024; Vichare & Bagiya 2024; Ohtani et al. 2025; Venugopal et al. 2025). This article presents a plausible mechanism for the abrupt change in IMF components around 22:05 UT, as observed by multiple satellites near the Sun-Earth L1 point. Fleet of space observatories during this unique event provided unprecedented in-situ observations from different vantage points using a total of seven spacecraft: NASA’s ACE, Wind, DSCOVR, STEREO-A, ARTEMIS-P2, MMS, and recently launched Indian Space Research Organization’s first observatory-class solar mission: Aditya-L1, revealing that the reconnection was triggered in the interior of an ICME MC, possibly due to the compression by adjacent ICME MC and quasisteady throughout the observation time. The prominent electron and ion flux enhancements, along with the suprathermal electron pitch angle distribution from the Wind spacecraft, complement the inference. Moreover, we attempted to provide an underlying physical mechanism of the occurrence of magnetic reconnection, utilizing multispacecraft observations. In the following three sections, data, methods, detailed observations, and in-depth discussions are presented.

2. DATA AND METHODS

This study uses in situ measurements from multiple upstream solar wind vantage points. From NASA’s Advanced Composition Explorer (ACE), we use Level-2 data: 16-second cadence magnetic field measurements (Smith et al. 1998) and 64-second cadence plasma parameters from SWEPAM (McComas et al. 1998). Magnetic field data from ISRO’s Aditya-L1 fluxgate magnetometer (Yadav et al. 2025) are included. Wind mission observations from the Three-Dimensional Plasma and Energetic Particle Investigation (Lin et al. 1995) and Magnetic Field Instrument(3-sec) (Lepping et al. 1995) are used for plasma moments, particle omnidirectional flux, suprathermal electron pitch angle distributions (PAD), and magnetic fields, respectively. NASA’s DSCOVR magnetic field(1-sec) and plasma moments

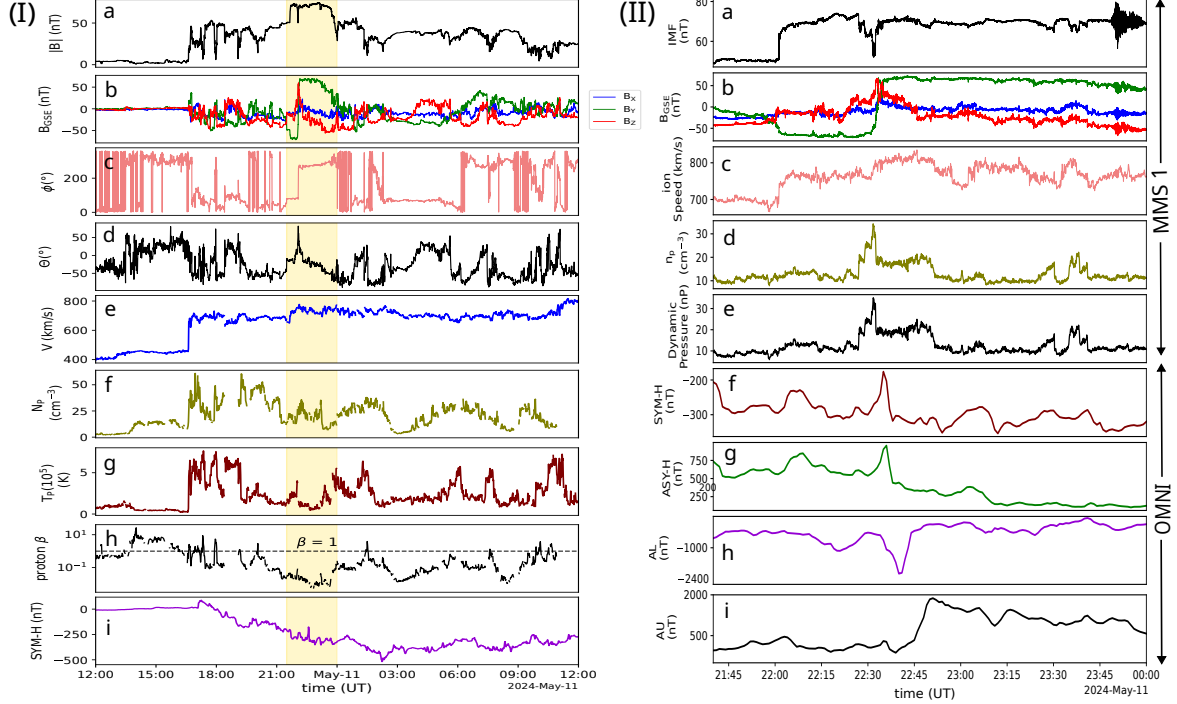


Figure 1. Panel(I) displays the observations recorded by the ACE spacecraft from May 10, 12:00 to 23:59:59 UT. Subpanels a to i represent IMF intensity, IMF components, IMF azimuth, elevation, solar wind bulk velocity, proton density, temperature, plasma beta (proton), and Sym-H. The yellow-shaded region marks the region of interest. Panel(II) shows MMS1 and OMNI data of the highlighted region of panel(I) with additional information about dynamic pressure, ASY-H, AL, and AU indices related to geomagnetic storms.

are obtained from the PlasMag suite (Burt & Smith 2012). THEMIS fluxgate magnetometer data (Angelopoulos 2008; Auster et al. 2008) are also incorporated. Additionally, Level-1 magnetic field measurements (8 Hz) from the STEREO-Ahead spacecraft are used, obtained from the IMPACT suite’s magnetic field experiment (Acuña et al. 2008; Kaiser et al. 2008). For near Earth’s magnetopause observation, we have utilized MMS1 fluxgate magnetometer (Russell et al. 2016) survey data (8 samples/s), Fast Plasma Instrument (FPI) (Pollock et al. 2016), Dual ion Spectrometer fast mode data for plasma moments, and OMNI data for geomagnetic indices.

In addition to plasma and magnetic field data analysis, Minimum Variance Analysis (MVA) and 2D-hodograms of the magnetic field (see Section A.1) are used to infer magnetic flux rope geometry and orientation (see Appendix section A.2 for more details).

3. OBSERVATIONS AND ANALYSIS

3.1. Overview of the Event

On May 10, 2024, Earth experienced a severe G5-class geomagnetic storm (Hayakawa et al. 2025; Thampi et al. 2025), triggered by multiple coronal mass ejections (CMEs). Figure 1 panel(I) highlights NASA’s Advanced Composition Analyser (ACE) solar wind data in the Geocentric Solar Ecliptic (GSE) frame. At 16:37 UT, the ICME shock arrival is marked by a sudden increase in interplanetary magnetic field (IMF) to 50 nT, solar wind velocity jump to 750 km/s, plasma density rising above 50 particles per cm^3 , and proton temperature exceeding 0.5 million Kelvin. The subsequent ICME sheath featured turbulent magnetic fields, elevated density, and temperature, with possible interaction regions. In a recent study, Weiler et al. (2025) reported preceding CMEs before 20:00 UT using ACE and STEREO-A data. This study focuses on 21:40 to 23:59 UT on May 10 (highlighted in yellow, in figure 1), showing constant $|\vec{B}|$ of 75 nT, followed by a sharp decrease at 22:04 UT, an abrupt rotation of the B_y from -70 nT to +75 nT, and B_z reversal. The decrease in plasma density and temperature, and plasma β (the ratio of thermal to magnetic pressure), suggests the highlighted region corresponds to an ICME MC. Figure 1 panel(II)h and i reports increased auroral Eastward (AL index) and Westward currents (AU index) at that time, indicating enhanced coupling between

solar wind-magnetosphere-ionosphere. The enhancement in SYM-H(e) and ASY-H(f) at 22:30 UT suggests a sudden amplification of the magnetopause current by a few hundred nT, due to localized high density and solar wind dynamic pressure.

3.2. Multipoint signatures of magnetic reconnection

Besides NASA's observatories at the Sun-Earth L1 point, the ADITYA-L1 mission of ISRO is the latest edition (Tripathi et al. 2022). All spacecraft monitor the upstream solar wind conditions with high-precision instruments. Leveraging spacecraft positions along the GSE-y direction (dawn-dusk), we investigated the region of interest in figure 1 spatially. We comprehensively analyzed plasma data from DSCOVR, ACE, and Wind. Due to the unavailability of plasma data, Aditya L1 observations could not be used. Figure 2 represents magnetic field and plasma moments data transformed into a boundary-normal frame using Minimum Variance Analysis (MVA) (Sonnerup & Cahill 1967). From 21:50 UT to 22:25 UT, all three spacecraft exhibited consistent observations with timing offsets due to separation of the spacecrafts along the GSEx direction (please refer to Appendix D). A systematic decrease in the minimum magnetic field magnitude ($|B|_{min}$) and a sharp rotation in the B_L component were observed along the dawn-dusk line. Concurrently, a localized dip followed by an increase in the L component of solar wind ion velocity (V_{iL}) was detected, with the width of the velocity dip decreasing progressively from DSCOVR to Wind. Further, density (n) and temperature (T) showed a localized order-of-magnitude increase across all three spacecraft. These observations indicate active magnetic reconnection and the presence of a current sheet (CS). The V_{iL} enhancement near the magnetic reversal matches the reconnection outflow signature, with bulk flow speed reaching up to 200 km/s along L, twice the background velocity. Observations suggest that all three spacecraft have traversed different spatial regions within the same reconnection outflow.

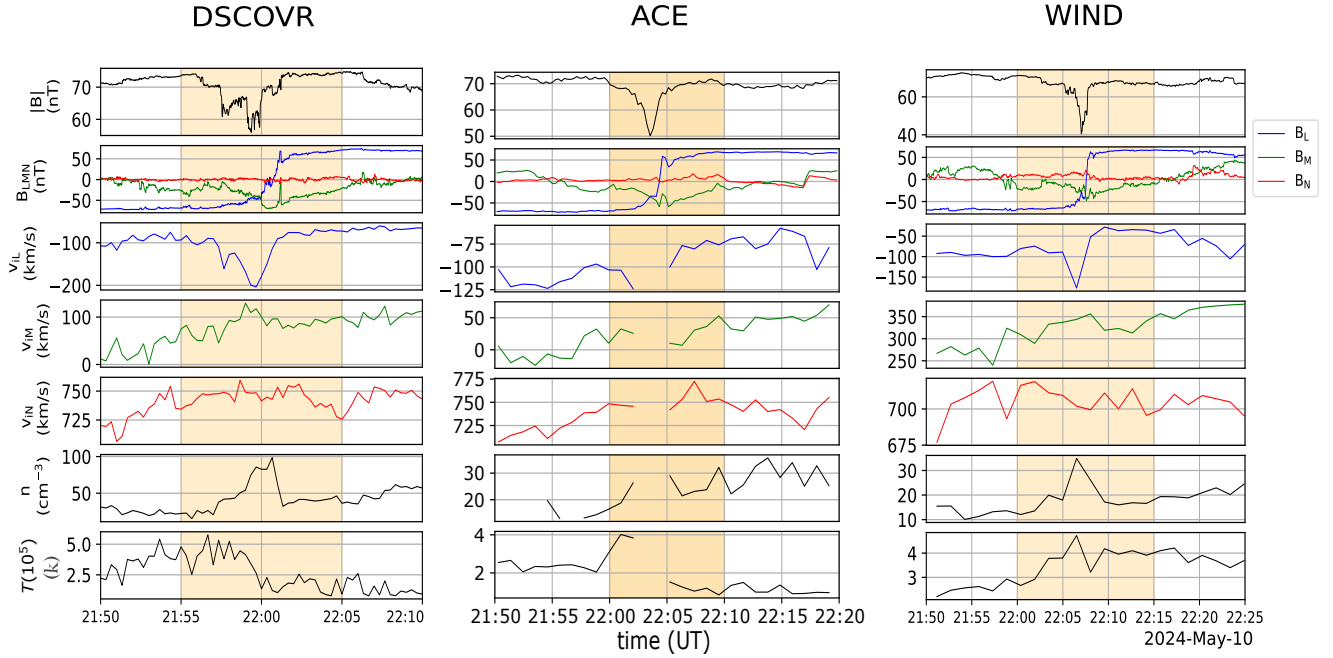


Figure 2. Comparison of DSCOVR, ACE, and Wind data during the ICME flux rope interval. Panels display the IMF magnitude, its components, solar wind velocity components, density, and temperature in a boundary normal coordinate system (LMN). The gaps in ACE observations are due to the unavailability of observations.

To quantify the reconnection outflow spatial scales and construct its geometry, plasma parameters were derived from in situ electron and proton plasma moments from DSCOVR, Wind, and ACE. The local plasma Debye length λ_d was ~ 5 meters ($\lambda_d = \sqrt{\epsilon K_B T_e / n_e e^2}$, where K_B , ϵ , T_e , n_e , represents Boltzmann constant, medium permittivity, electron temperature and density). The ion inertial length (d_i) was 15 km and electron inertial length (d_e) falls in the range of 595-600 meter ($d_{i(e)} = c / \omega_{pi(e)}$, where $\omega_{pi(e)}$ and c denote the ion(electron) plasma frequency and speed of light).

The electron and ion inertial lengths, or skin depths, define the characteristic scales beyond which electrons and ions decouple from the magnetic field. Given the high solar wind velocity, spacecraft velocities were deemed negligible. Therefore, using timing analysis, the width of the outflow jets was determined to be 26, 30, and 13 R_E (where 1 R_E = 6317 km) for DSCOVR, ACE, and Wind, respectively. Notably, the B_L component reversal and the outflow jet exhibit consistent directional alignment along -ve L (or GSEy), indicating the current sheet orientation is closely aligned with the GSE-y axis. These results imply the reconnection diffusion region location was duskward of the Wind spacecraft. Using fluxgate magnetometer data from Aditya-L1 spacecraft (Yadav et al. 2025), located 100 R_E dawnward, the current sheet's spatial extent was estimated at $\sim 203 R_E$. Although Aditya-L1's plasma data is unavailable for this exercise, its unique location enabled us to determine the maximum observable length of the reconnection outflow based on its magnetometer data. Therefore, the spatial separation of all the L1 observatories and near-simultaneous observations enables us to construct the reconnection geometry, which is explained in the discussion section.

In magnetic reconnection, magnetic energy is efficiently converted into plasma kinetic energy, accelerating charged particles, particularly within the outflow jets, where particles can attain relativistic speeds. Using the Three-dimensional plasma and Energetic Particle Investigation Instrument (Lin et al. 1995) aboard the Wind mission, the electron and ion omnidirectional energy flux spectrogram is displayed in figure 3b. We observe a significant enhancement in ion energy, reaching up to 10 keV, compared to the background energy band of 2-4 keV. The electron energy spectrum also exhibits a noticeable flux amplification by an order of magnitude between 22:05 UT and 22:10 UT. Hence, it is evident that notable particle energization has taken place, coinciding with the B_{min} position. Moreover, the ion flux displays a distinct band centered around 6-8 keV, which is twice the energy of observed protons and can be attributed to the presence of helium ions. Studies have shown that MC internal magnetic reconnections often disrupt the coherence of the flux tube (Farrugia et al. 2023), leading to flux erosion (Pal et al. 2020). Carcaboso et al. (2020) have characterized the pitch-angle-distribution (PADs) of solar wind suprathermal electrons, highlighting their significance in diagnosing the magnetic topology. A key finding of the study depicts that bidirectional PADs indicate closed magnetic structures, while isotropic distributions suggest disconnection by magnetic reconnection or highly turbulent sheaths. In this present case, we observed high field-aligned electron flux throughout the region of interest, except at the B_{min} point, which indicates isotropic PADs, suggesting a disconnected field line due to reconnection. These observations provide compelling evidence to conclude the presence of an ongoing magnetic reconnection within the flux rope and particle acceleration in its outflow regions.

4. DISCUSSION

ICME flux rope magnetic fields are often modeled as twisted circular cross-sections (see e.g. Gómez-Herrero et al. (2017)); although it may not hold in reality (Al-Haddad et al. 2011). In 1974, J.B. Taylor showed that Reversed Field Pinches (RFP) relax to a minimum-energy Taylor state via magnetic reconnection (Taylor 1974), satisfying $\nabla \times \mathbf{B} = \lambda \mathbf{B}$ with constant λ . If magnetic flux $\Phi = \int_A \vec{B} \cdot d\vec{n}$ and helicity $K = \int_V \vec{A} \cdot \vec{B} d\tau$ (A is magnetic vector potential) are invariant in RFP geometry, relaxation occurs through reconnection (Taylor 1986). Approximately, solar flux ropes can be considered to originate in a force-free state (Burlaga et al. 1981; Lepping et al. 1990), though not always (Xie et al. 2023). Deviations from the Taylor state in the interplanetary medium may trigger reconnection. Reconnection signatures inside ICME flux ropes have been observed previously by Gosling et al. (2005, 2006). In a pioneering work, Fermo et al. (2014) demonstrated the occurrence of reconnection in a stretched or elongated flux rope through numerical simulation, motivating our effort to link such evidence to the reconnection origin in this study.

The diverse spatial distribution of the spacecrafts (figure 7) provided a unique opportunity for examining the spatiotemporal evolution of the MCs (MC identification criteria are presented in Appendix B). STEREO-A (Kaiser & Adams 2007), positioned 1798 R_E sunward (GSE_x) and 4907 R_E dawnward ($-GSE_y$), observed the event 3.24 hour before ACE. Two distinct magnetic regions, E1 and E2 (antique white and magenta in figure 4a), having similar IMF intensity, are separated by an interaction region (May 10, 19:40-20:06 UT) marked by abrupt magnetic fluctuations. Minimum Variance Analysis (MVA, details in Appendix A.2) and 2D hodogram of STEREO-A data reveal that E1 exhibits a coherent, large-scale magnetic rotation, with a smooth color gradient in the $\phi - \theta$ plot (figure 4c) and an elevation change from $+75^\circ$ to -75° across a full $0^\circ - 360^\circ$ azimuth span. This suggests a well-developed flux rope with an almost perpendicular orientation ($\theta_{max} = 89.98^\circ$). The hodogram's arc pattern further supports this interpretation. In contrast, E2 displays a different orientation ($\theta_{max} = 63.68^\circ$) and reduced coherence, possibly indicating a distorted structure (not shown in plot). However, the lack of STEREO-A plasma data precludes definitive

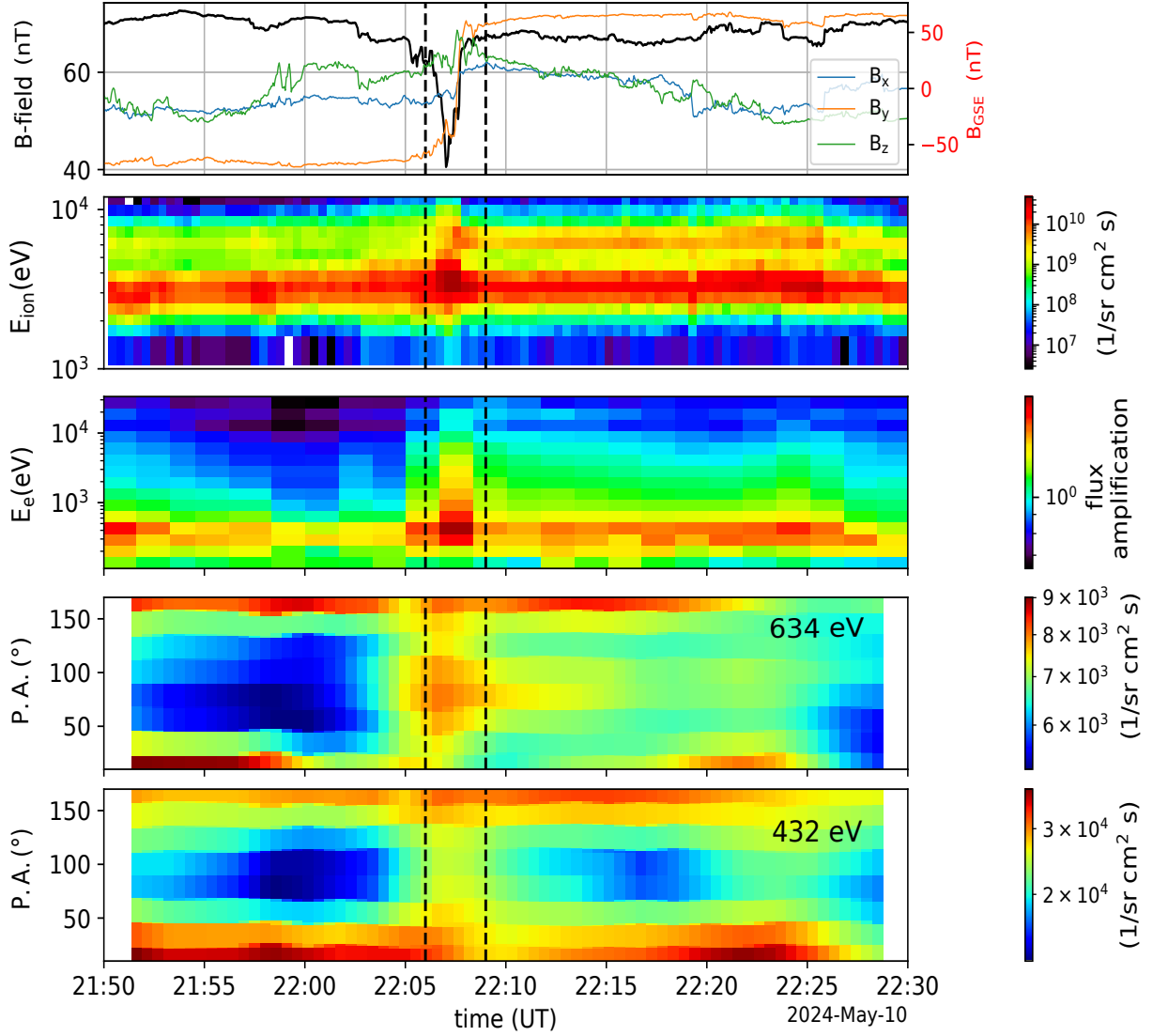


Figure 3. This figure shows from the top timeseries data of: IMF magnitude (B-field) and components, solar wind ion energy spectrogram (E_{ion}), electron energy spectrogram (E_e , normalized by 21:00 UT flux, outside the MC), and solar wind suprathermal electron pitch angle distribution (634 & 432 eV) respectively from 21:50 UT to 22:30 UT on May 10 from Wind spacecraft data. The other suprathermal electron channels (> 60 eV) show similar behavior. The white bands represent data gaps. Two black vertical lines mark the region of interest.

classification. Notably, E1 shows no significant sharp decrease in IMF intensity.

At L1, ACE observed a similar B_N and B_T variation to STEREO-A, though in a more compressed form, with the two structures (E1 and E2) appearing substantially overlapped. In figure 4a, the STEREO-A MC interval (black dotted horizontal line) corresponds to a compressed section in the ACE data (red arrow). At the same time, the trailing portion of E2 remains detectable visually (black arrow). Comparable durations of E1 and E2 in both datasets suggest interacting or sequentially merging flux ropes. MVA and 2D hodogram analysis of ACE data (21:40-23:59 UT, May 10; figure 4d) reveal a discontinuous $\phi - \theta$ relation, contrasting with the smooth STEREO-A flux rope signature. The limited elevation range, partial azimuth coverage, and temporal discontinuities may imply intermittent reconnection, though alternative explanations include a partially developed flux rope or short-duration crossing. The pronounced $|\vec{B}|$ drop supports the presence of an internal reconnection region. Consistent findings are obtained from other L1

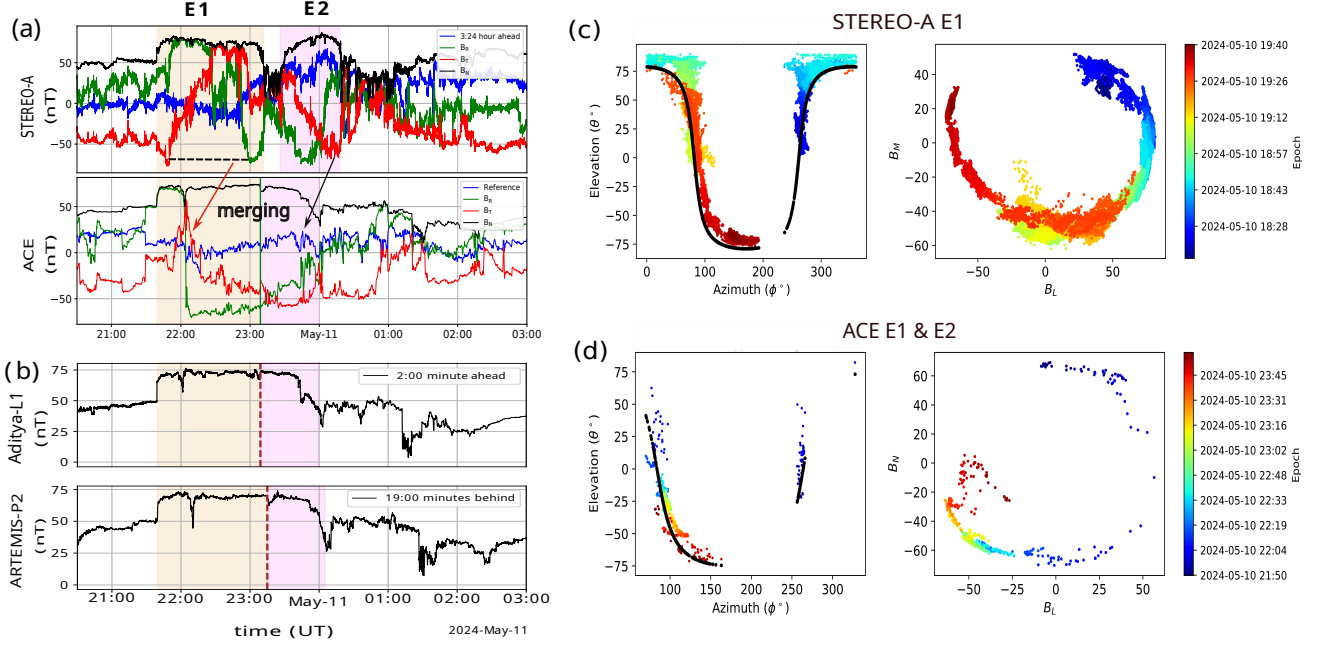


Figure 4. The timeshifted magnetic field observation from STEREO-A to match the MC initiation at 21:39:22 UT with ACE in panel (a) in RTN coordinates, followed by ADITYA-L1 and THEMIS-C/ARTEMIS P2 observation of the reconnection, respectively. The areas marked in antique white and magenta are two successive Ejectas/MCs, E1 and E2. Panel (c) & (d) describes the azimuth vs elevation angle and 2D magnetic field hodogram result from MVA analysis of STEREO-A and ACE magnetic field data corresponding to E1 MC.

spacecraft (see Appendix A.2). Between L1 and ARTEMIS-P2, θ_{max} further decreases from $\sim 80^\circ$ to $\sim 54.79^\circ$, while λ_2/λ_3 increases from 16 to 40 (table 2), indicating a rotation of the boundary normal relative to the upstream field and a more well-defined planar boundary. This behavior is consistent with, though not uniquely diagnostic of, progressive flattening (‘pancaking’) of the magnetic cloud during propagation (Raghav et al. 2023).

The cross-section of ICME MC rapidly flattens or pancakes, losing its coherence, owing to the radial expansion (Owens et al. 2017, 2005). Moreover, large-scale current sheets and subsequent magnetic reconnection can trigger inside MCs due to the deformation (Owens 2009; Fermo et al. 2014). Therefore, we argue that due to the interaction and merging of E1 & E2 between STEREO-A and L1 position, E1 became compressed, which might have led to deviation from the Taylor state and induced internal reconnection within E1, specifically involving the B_T component of its internal surface magnetic field, facilitated by the formation of a current sheet. This internal MC reconnection was observed by Aditya L1, two minutes before ACE, and subsequently by DSCOVR, ACE, Wind, ARTEMIS P2 (figure 4b). This temporal sequence indicates the quasi-steady nature of the ongoing reconnection for at least 35 minutes, including MMS observation near the magnetopause. An artistic illustration describing this observational scenario is presented in figure 5a, where the spacecraft positions used in the analysis are schematically represented in figure 5a. Figure 5b provides a cross-sectional view of the intricate flux rope interaction and the ongoing magnetic reconnection between the surface magnetic fields. The reconnection geometry is shown in GSE coordinates with all the L1 spacecraft crossings schematically in figure 5c.

While the above physical picture explains the observations, the solution is not unique and depends on underlying assumptions. A possible alternative is a geometric effect: STEREO-A and ACE were separated in the $L(GSE_y)$ direction by over $4000 R_E$. Given the propagation of the two MCs, merging or interaction may have occurred at the Earth-directed section, distant from STEREO-A. The absence of STEREO-A plasma data limits detailed analysis of E1 and E2. If E1 and E2 at ACE represent a single flux rope, the interaction or merging hypothesis would be invalid, favouring deformation and compression instead. However, the Wind spacecraft electron and ion omnidirectional energy, along with suprathermal electron fluxes, reveal contrasting evidence between E1 AND E2 (figure 6), indicating disparate

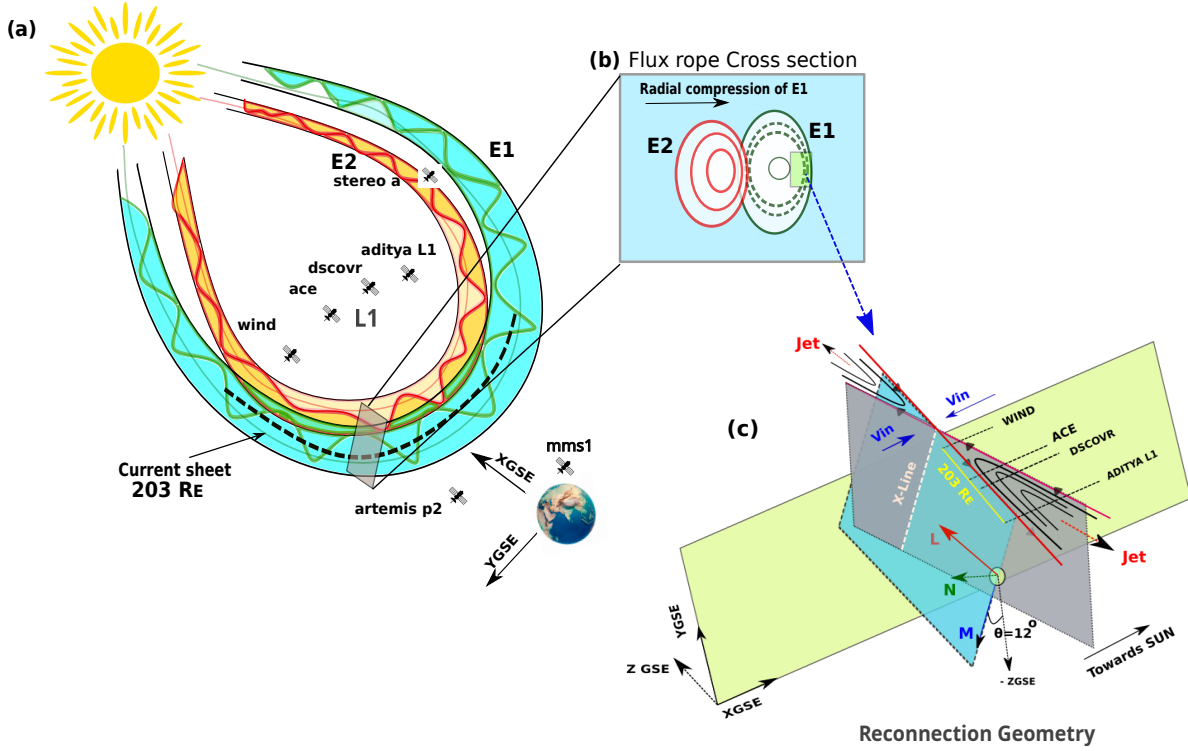


Figure 5. Artistic illustration of the ICME-ICME interaction and embedded magnetic reconnection site. Panel (a) describes the interaction of two ICME MCs on May 10, 2024. Two prominent MCs (E1 & E2) are marked with green and yellow, respectively, in the GSE coordinate system, with all the tentative positions of the spacecraft (Appendix D). The internal magnetic reconnection current sheet is marked in a black dashed line inside E1 MC spanning $203 R_E$ along the dawn-dusk direction. Panel (b) represents the cross-sectional view of the reconnection site, indicating the structural deformation of E1 due to intense compression from the trailing MC E2. Panel (c) displays the 3D reconnection geometry in the GSE and local Boundary normal coordinate system (LMN, Appendix A.1). All spacecraft around the L1 point probed the same reconnection outflow jet. The ecliptic plane is visualized in green, while the sky blue plane represents the plane containing the reconnection X-LINE, which is along the M direction, inclined to -ZGSE at an angle of 12° . This sketch is for illustration purposes only and not to scale.

plasma behaviour and supporting the merging of two MCs. Although magnetic field signatures alone cannot separate the structures, plasma data provide a complementary perspective. Moreover, a solar wind bulk speed increase behind the E1-E2 boundary (figure 1Ie) suggests compression from ICME-ICME interaction, inhibiting E1's expansion (Russell & Shinde 2005). Thus, multispacecraft observations indicate reconnection initiated by merging MCs via current sheet formation, and its impact caused rapid changes in the magnetosphere-ionosphere system. Future numerical modeling could further substantiate this interpretation.

5. ACKNOWLEDGEMENT

The authors express their sincere gratitude to the ACE, DSCOVR, Wind, STEREO, MMS, and THEMIS mission teams of NASA and ISRO's Aditya-L1 for their dedicated efforts in operating the missions and for providing high-quality scientific data in the public domain. S.B. appreciates the financial support provided by the Indian Space Research Organization through a research grant. The magnetic field and plasma data of NASA's ACE, Wind, DSCOVR, and ARTEMIS-P2 & STEREO-A are publicly available on the following website: <https://cdaweb.gsfc.nasa.gov/>. One can visit the science gateways of all the spacecraft mentioned above to check the current data availability. The ADITYA L1 mission data are available at: <https://www.isdc.gov.in/aditya1.html>. The Python-based Space Physics Environment Data Analysis Software (pySPEDAS) (<https://github.com/spedas/pyspedas>) has been used to analyze and plot the mission data.

APPENDIX

A. METHODS

A.1. Boundary Normal Coordinate (LMN) determination.

Minimum Variance Analysis (Sonnerup & Cahill (1967)) has been used to transform the in-situ data from the GSE coordinate system to the boundary normal coordinate system. In the GSE coordinate basis, the new coordinate system components are $L = [0.61615, 0.98312, 0.08625]$, $M = [-0.1717, 0.11404, -0.97851]$, $N = [-0.97183, 0.14306, 0.18727]$. The pySPEDAS module has been used to determine the minimum variance matrix and then applied to the data to transform them from GSE to LMN coordinates. For further details, please refer to the GitHub tutorials of pySPEDAS (link provided in Acknowledgement)

LMN	Angle to XGSE	Angle to YGSE	Angle to ZGSE
L	80.71°	10.54°	85.05°
M	99.89°	83.45°	168.36°
N	166.36°	81.77°	79.20°

Table 1. Orientation of Reconnection LMN to GSE coordinate

A.2. Minimum Variance analysis and 2D hodogram.

When magnetic field $\vec{B} = (B_x, B_y, B_z) = (B \cos \theta \cos \phi, B \cos \theta \sin \phi, B \sin \theta)$, are parallel to a plane having normal $n = (n_x, n_y, n_z)$ (where θ and ϕ are azimuthal and inclination angles of magnetic field vector respectively), the relation between θ and ϕ is given by Nakagawa et al. (1989); Nakagawa (1993); Palmerio et al. (2016)

$$n_x \cos \theta \cos \phi + n_y \cos \theta \sin \phi + n_z \sin \theta = 0 \quad (A1)$$

The above curve fitting to the measured θ and ϕ distribution in $\phi - \theta$ space indicates the presence of a Planar Magnetic Structure (PMS). To check the planarity of the vector in 2D, $|B_n|/B$ is calculated, where B is the magnitude of the IMF and B_n is a component of the magnetic field normal to the PMS plane. The PMS will be in a perfect plane when $B_n \approx 0$. Therefore, a low value of $|B_n|/B$ indicates the vector is parallel to a plane.

The Minimum Variance Analysis (MVA) technique is used to identify the orientation and the normal of a magnetic field structure. The MVA analysis for the selected region estimates three new directions as maximum (B_L), intermediate (B_M), and minimum (B_N) variances corresponding to maximum (λ_1), intermediate (λ_2), and minimum (λ_3) eigenvalues and three eigenvectors ($\hat{n}_1, \hat{n}_2, \hat{n}_3$), respectively (Sonnerup & Cahill 1967; Palmerio et al. 2016). Here, $\hat{n}_3 = \hat{n}$ represents the normal to the plane. The ratio of the intermediate to minimum eigenvalue ($R = \lambda_2/\lambda_1$) indicates the efficiency of the MVA technique (Shaikh et al. 2018). The MVA time intervals are shown below. The identification of planar magnetic structures is presented in detail in Nakagawa et al. (1989); Neugebauer et al. (1993); Palmerio et al. (2016); Shaikh et al. (2018). Generally, smooth rotation of magnetic field components i.e arc or semicircular pattern

in one of the planes ($B_L - B_M$, $B_L - B_N$, $B_M - B_N$) indicates rotational structures of magnetic fields (Khabarova et al. 2015; Shaikh et al. 2017) in 2D hodogram plot.

B. MAGNETIC CLOUD SELECTION CRITERIA AND INTERVALS

In this study, we utilized the basic criteria for Magnetic cloud identification using magnetic field and plasma parameters. The STEREO-A MC E1 and E2 have been identified based on (1) enhanced magnetic field compared to surroundings (> 10 nT); (2) smooth rotation of magnetic field components over a large angle. Further, E1 and E2 were well separated by a highly fluctuating magnetic field, indicating an interaction region. However, due to the non-availability of plasma data from STEREO-A, we are unable to check plasma beta and temperature, which are essential parameters for MC identification. Still, Minimum Variance Analysis and 2D hodogram analysis enabled us to identify the E1 & E2 (with $\theta_{max}=89.98$ and 63.68 , respectively) region to be a well-developed and deformed flux rope, respectively.

At L1, ACE observation indicates a single MC instead of E1 and E2 separately. With the help of the magnetic field of ACE only, we cannot distinguish them. But there is specific observational evidence that highlights the merging of E1 and E2 at L1. These are:

1. Using magnetic field data and comparing the time duration of E1 and E2 between STEREO-A and ACE: quantitatively, the time duration of STEREO-A E1 & E2 and their ACE counterpart is similar (approximately 2:20 hours). This also suggests the expansion of E1 due to high compression. Moreover, the magnetic field orientation (2024-05-10/21:39:00 to 23:59:00 UT) resembles that of STEREO-A E1 in a compressed manner. The trailing portion of E2 can also be identifiable (figure 4).

2. From Plasma Observation using Wind: The above explanation is not sufficient to identify the E1 and E2 regions at L1. To further support our inference, we utilized electron, ion energy flux, and suprathermal electron pitch angle distributions (PADs) data. We notice distinct changes in the spectrograms and PADs after 2024-05-10/23:09:00 UT (boundary between E1 and E2).

All other observatories at L1 show similar evidence, and MC boundaries have been identified based on timing analysis. Therefore, we concluded the merging of two ICME MCs at L1 and used the E1 & E2 intervals for MVA analysis (apart from STEREO-A).

Start (UT)	End (UT)	Event	MVA analysis results
2024-05-10/18:15:00	2024-05-10/19:40:00	STEREO-A MC E1	$\theta_{max} = 89.98$, $\langle B_n \rangle / \langle B \rangle = 0.41$, $\lambda_2/\lambda_3 = 63.31$
2024-05-10/20:06:00	2024-05-10/20:53:00	STEREO-A MC E2	$\theta_{max} = 63.68$, $\langle B_n \rangle / \langle B \rangle = 0.52$, $\lambda_2/\lambda_3 = 3.08$
2024-05-10/21:37:00	2024-05-10/23:57:00	Aditya-L1 MC E1 & E2	$\theta_{max} = 73.34$, $\langle B_n \rangle / \langle B \rangle = 0.76$, $\lambda_2/\lambda_3 = 37.71$
2024-05-10/21:36:00	2024-05-10/23:55:35	DSCOVR MC E1 & E2	$\theta_{max} = 80.11$, $\langle B_n \rangle / \langle B \rangle = 0.66$, $\lambda_2/\lambda_3 = 31.02$
2024-05-10/21:39:00	2024-05-10/23:59:00	ACE MC E1 & E2	$\theta_{max} = 82.24$, $\langle B_n \rangle / \langle B \rangle = 0.68$, $\lambda_2/\lambda_3 = 26.96$
2024-05-10/21:45:00	2024-05-10/23:40:00	Wind MC E1 & E2	$\theta_{max} = 82.98$, $\langle B_n \rangle / \langle B \rangle = 0.70$, $\lambda_2/\lambda_3 = 16.53$
2024-05-10/21:58:00	2024-05-11/00:19:00	Artemis-P2 MC E1& E2	$\theta_{max} = 54.79$, $\langle B_n \rangle / \langle B \rangle = 0.69$, $\lambda_2/\lambda_3 = 40.36$

Table 2. Time intervals of MVA analysis. The columns represent the start and end time of E1 and E2 MCs detected by the spacecrafts mentioned, and the Minimum variance analysis results, respectively. θ_{max} , $\langle B_n \rangle / \langle B \rangle$, and λ_2/λ_3 provide a rough orientation of the flux rope, presence of magnetic field along the direction normal to the flux rope boundary, and the quality or reliability of the MVA result, respectively.

C. WIND MAGNETIC CLOUD FLUX AND PITCH ANGLE

D. SPACECRAFT POSITIONS

REFERENCES

Acuña, M., Curtis, D., Scheifele, J., et al. 2008, Space Science Reviews, 136, 203,
doi: [10.1007/978-0-387-09649-0_8](https://doi.org/10.1007/978-0-387-09649-0_8)

Al-Haddad, N., Roussev, I. I., Möstl, C., et al. 2011, The Astrophysical Journal Letters, 738, L18,
doi: [10.1088/2041-8205/738/2/L18](https://doi.org/10.1088/2041-8205/738/2/L18)

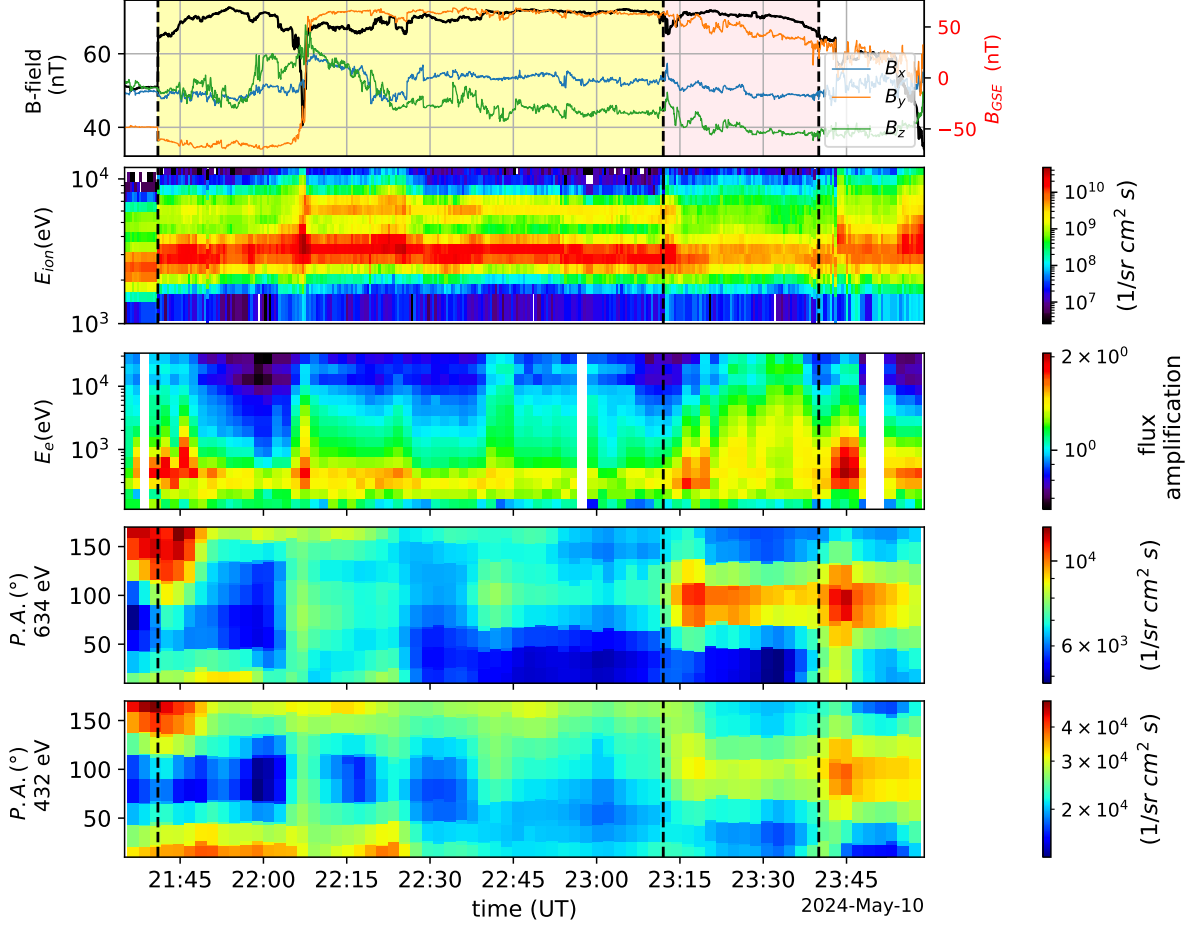


Figure 6. Wind spacecraft observation of the complex magnetic cloud structure. Panels display the magnetic field, ion, and electron omnidirectional energy flux, as well as the suprathermal electron pitch angle distribution, in two separate channels. The yellow and pink shaded regions represent two different flux ropes.

Spacecraft	XGSE (R_E)	YGSE (R_E)	ZGSE (R_E)
ACE	223.77	3.35	22.44
Wind	215.75	100.99	-0.93
DSCOVER	244.46	-28.49	20.26
ARTEMIS P2	46.69	36.48	5.49
Aditya-L1	232.67	-102.12	8.42
STEREO-A	1798.6	-4906.5	24.3
MMS	11.66	-19.27	-5.50

Table 3. GSE coordinates of spacecrafts on 10th May 2025 at 22:00 UT

Angelopoulos, V. 2008, Space Science Reviews, 141, 5,
doi: [10.1007/978-0-387-89820-9_2](https://doi.org/10.1007/978-0-387-89820-9_2)

Ashna, V., Bhaskar, A., Manju, G., & Sini, R. 2024,
Journal of Geophysical Research: Space Physics, 129,
e2023JA031687, doi: [10.1029/2023ja031687](https://doi.org/10.1029/2023ja031687)

Auster, H., Glassmeier, K., Magnes, W., et al. 2008, Space
science reviews, 141, 235,
doi: [10.1007/978-0-387-89820-9_11](https://doi.org/10.1007/978-0-387-89820-9_11)

Burlaga, L., Sittler, E., Mariani, F., & Schwenn, a. R. 1981,
Journal of Geophysical Research: Space Physics, 86,
6673, doi: [10.1029/ja086ia08p06673](https://doi.org/10.1029/ja086ia08p06673)

Burt, J., & Smith, B. 2012, IEEE, 1

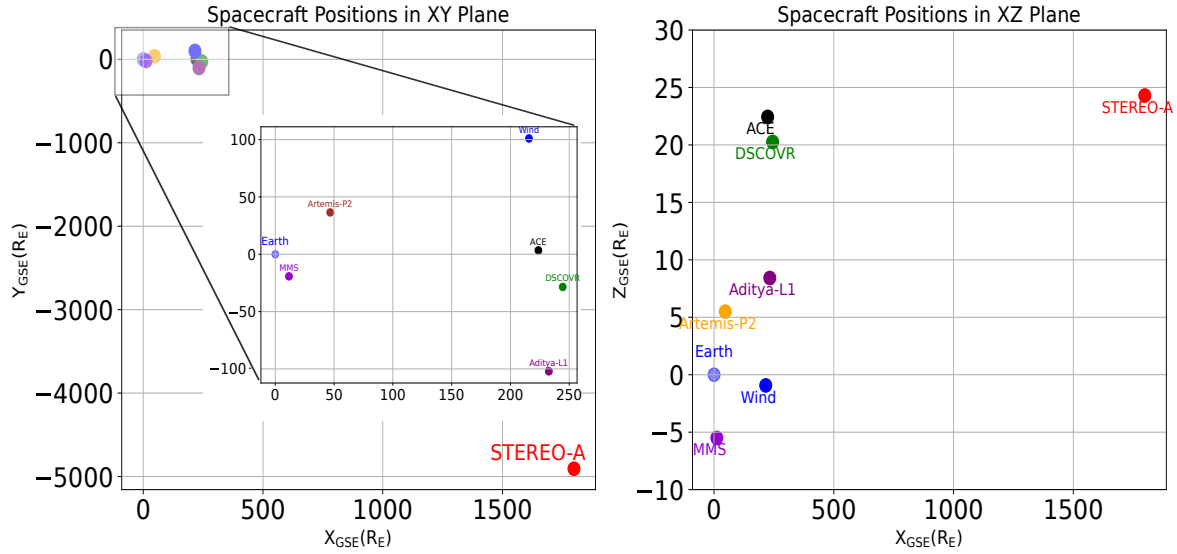


Figure 7. Spacecraft positions in Geocentric Solar Ecliptic (GSE) Coordinate System on 10th May 2025 at 22:00 UT

- Carcaboso, F., Gómez-Herrero, R., Lara, F. E., et al. 2020, *Astronomy & Astrophysics*, 635, A79, doi: [10.1051/0004-6361/201936601](https://doi.org/10.1051/0004-6361/201936601)
- Chakrabarty, D., Hui, D., Rout, D., et al. 2017, *Journal of Geophysical Research: Space Physics*, 122, 2574, doi: [10.1002/2016ja022781](https://doi.org/10.1002/2016ja022781)
- Farrugia, C., Vasquez, B., Lugaz, N., et al. 2023, *The Astrophysical Journal*, 953, 15, doi: [10.3847/1538-4357/acdcf7](https://doi.org/10.3847/1538-4357/acdcf7)
- Fermo, R. L., Opher, M., & Drake, J. F. 2014, *Physical Review Letters*, 113, 031101, doi: [10.1103/physrevlett.113.031101](https://doi.org/10.1103/physrevlett.113.031101)
- Fu, W., Fu, H., Zhang, W., Yu, Y., & Cao, J. 2025, *Geophysical Research Letters*, 52, e2024GL114040, doi: [10.1029/2024gl114040](https://doi.org/10.1029/2024gl114040)
- Gómez-Herrero, R., Dresing, N., Klassen, A., et al. 2017, *The Astrophysical Journal*, 840, 85, doi: [10.3847/1538-4357/aa6c5c](https://doi.org/10.3847/1538-4357/aa6c5c)
- Gonzalez, W., Joselyn, J.-A., Kamide, Y., et al. 1994, *Journal of Geophysical Research: Space Physics*, 99, 5771, doi: [10.1029/93ja02867](https://doi.org/10.1029/93ja02867)
- Gonzalez, W., & Parker, E. 2016, *Astrophysics and space science library*, 427, 10, doi: [10.1007/978-3-319-26432-5](https://doi.org/10.1007/978-3-319-26432-5)
- Gonzalez, W. D., Echer, E., Tsurutani, B. T., Clúa de Gonzalez, A. L., & Dal Lago, A. 2011, *Space science reviews*, 158, 69, doi: [10.1007/s11214-010-9715-2](https://doi.org/10.1007/s11214-010-9715-2)
- Gopalswamy, N. 2016, *Geoscience Letters*, 3, 1, doi: [10.1186/s40562-016-0039-2](https://doi.org/10.1186/s40562-016-0039-2)
- Gosling, J., Eriksson, S., Skoug, R. M., McComas, D., & Forsyth, R. 2006, *The Astrophysical Journal*, 644, 613, doi: [10.1086/503544](https://doi.org/10.1086/503544)
- Gosling, J., Hildner, E., MacQueen, R., et al. 1974, *Journal of Geophysical Research*, 79, 4581, doi: [10.1029/ja079i031p04581](https://doi.org/10.1029/ja079i031p04581)
- Gosling, J., Pizzo, V., & Bame, S. J. 1973, *Journal of Geophysical Research*, 78, 2001, doi: [10.1029/ja078i013p02001](https://doi.org/10.1029/ja078i013p02001)
- Gosling, J., Skoug, R. M., McComas, D., & Smith, C. 2005, *Journal of Geophysical Research: Space Physics*, 110, doi: [10.1029/2004ja010809](https://doi.org/10.1029/2004ja010809)
- Hapgood, M. 2017, *Space weather* (IOP Publishing), doi: [10.1088/978-0-7503-1372-8ch1](https://doi.org/10.1088/978-0-7503-1372-8ch1)
- Hayakawa, H., Ribeiro, P., Vaquero, J. M., et al. 2020, *The Astrophysical Journal Letters*, 897, L10, doi: [10.3847/2041-8213/ab6a18](https://doi.org/10.3847/2041-8213/ab6a18)
- Hayakawa, H., Ebihara, Y., Mishev, A., et al. 2025, *The Astrophysical Journal*, 979, 49, doi: [10.3847/1538-4357/ad9335](https://doi.org/10.3847/1538-4357/ad9335)
- Hirshberg, J., Alksne, A., Colburn, D., Bame, S., & Hundhausen, A. 1970, *Journal of Geophysical Research*, 75, 1, doi: [10.1029/ja075i001p00001](https://doi.org/10.1029/ja075i001p00001)
- Holappa, L., Asikainen, T., & Mursula, K. 2020, *Geophysical Research Letters*, 47, e2019GL086676, doi: [10.1029/2019gl086676](https://doi.org/10.1029/2019gl086676)
- Holappa, L., Robinson, R., Pulkkinen, A., Asikainen, T., & Mursula, K. 2021, *Journal of Geophysical Research: Space Physics*, 126, e2021JA029202, doi: [10.1029/2021ja029202](https://doi.org/10.1029/2021ja029202)
- Kaiser, M. L., & Adams, W. J. 2007, *IEEE*, 1, doi: [10.1109/aero.2007.352745](https://doi.org/10.1109/aero.2007.352745)

- Kaiser, M. L., Kucera, T., Davila, J., et al. 2008, *Space Science Reviews*, 136, 5, doi: [10.1007/978-0-387-09649-0_2](https://doi.org/10.1007/978-0-387-09649-0_2)
- Khabarova, O., Zank, G., Li, G., et al. 2015, *The Astrophysical Journal*, 808, 181, doi: [10.1088/0004-637x/808/2/181](https://doi.org/10.1088/0004-637x/808/2/181)
- Khabarova, O., Malandraki, O., Malova, H., et al. 2021, *Space Science Reviews*, 217, 38, doi: [10.1007/s11214-021-00814-x](https://doi.org/10.1007/s11214-021-00814-x)
- Khabarova, O. V., Zank, G. P., Li, G., et al. 2016, *The Astrophysical Journal*, 827, 122, doi: [10.3847/0004-637x/827/2/122](https://doi.org/10.3847/0004-637x/827/2/122)
- Kilpua, E., Koskinen, H. E., & Pulkkinen, T. I. 2017, *Living Reviews in Solar Physics*, 14, 1, doi: [10.1007/s41116-017-0009-6](https://doi.org/10.1007/s41116-017-0009-6)
- Klein, L., & Burlaga, L. 1982, *Journal of Geophysical Research: Space Physics*, 87, 613, doi: [10.1029/ja087ia02p00613](https://doi.org/10.1029/ja087ia02p00613)
- Kruparova, O., Krupar, V., Szabo, A., et al. 2024, *The Astrophysical Journal Letters*, 970, L13, doi: [10.3847/2041-8213/ad5da6](https://doi.org/10.3847/2041-8213/ad5da6)
- Kwak, Y.-S., Kim, J.-H., Kim, S., et al. 2024, *Journal of Astronomy and Space Sciences*, 41, 171, doi: [10.5140/jass.2024.41.3.171](https://doi.org/10.5140/jass.2024.41.3.171)
- Lepping, R., Jones, J., & Burlaga, L. 1990, *Journal of Geophysical Research: Space Physics*, 95, 11957, doi: [10.1029/ja095ia08p11957](https://doi.org/10.1029/ja095ia08p11957)
- Lepping, R., Acuña, M., Burlaga, L., et al. 1995, *Space Science Reviews*, 71, 207
- Lin, R., Anderson, K., Ashford, S., et al. 1995, *Space Science Reviews*, 71, 125, doi: [10.1007/bf00751328](https://doi.org/10.1007/bf00751328)
- Manchester IV, W., Gombosi, T., De Zeeuw, D., et al. 2005, *The Astrophysical Journal*, 622, 1225, doi: [10.1086/427768](https://doi.org/10.1086/427768)
- Manchester IV, W. B., Gombosi, T. I., Roussev, I., et al. 2004, *Journal of Geophysical Research: Space Physics*, 109, doi: [10.1029/2002JA009672](https://doi.org/10.1029/2002JA009672)
- McComas, D., Bame, S., Barker, P., et al. 1998, *The advanced composition explorer mission*, 563, doi: [10.1007/978-94-011-4762-0_20](https://doi.org/10.1007/978-94-011-4762-0_20)
- Nakagawa, T. 1993, *Solar physics*, 147, 169, doi: [10.1007/bf00675493](https://doi.org/10.1007/bf00675493)
- Nakagawa, T., Nishida, A., & Saito, T. 1989, *Journal of Geophysical Research: Space Physics*, 94, 11761, doi: [10.1029/ja094ia09p11761](https://doi.org/10.1029/ja094ia09p11761)
- Neugebauer, M., Clay, D., & Gosling, J. 1993, *Journal of Geophysical Research: Space Physics*, 98, 9383, doi: [10.1029/93ja00216](https://doi.org/10.1029/93ja00216)
- Niembro, T., Lara, A., González, R. F., & Cantó, J. 2019, *Journal of Space Weather and Space Climate*, 9, A4, doi: [10.1051/swsc/2018049](https://doi.org/10.1051/swsc/2018049)
- Ohtani, S., Zou, Y., Merkin, V., et al. 2025, *Journal of Geophysical Research: Space Physics*, 130, e2024JA033691, doi: [10.1029/2024ja033691](https://doi.org/10.1029/2024ja033691)
- Owens, M. 2009, *Solar Physics*, 260, 207, doi: [10.1007/s11207-009-9442-6](https://doi.org/10.1007/s11207-009-9442-6)
- Owens, M., Lockwood, M., & Barnard, L. 2017, *Scientific Reports*, 7, 4152, doi: [10.1038/s41598-017-04546-3](https://doi.org/10.1038/s41598-017-04546-3)
- Owens, M. J., Cargill, P., Pagel, C., Siscoe, G., & Crooker, N. 2005, *Journal of Geophysical Research: Space Physics*, 110, doi: [10.1029/2004ja010814](https://doi.org/10.1029/2004ja010814)
- Pal, S., Dash, S., & Nandy, D. 2020, *Geophysical Research Letters*, 47, e2019GL086372, doi: [10.1029/2019GL086372](https://doi.org/10.1029/2019GL086372)
- Palmer, I., Allum, F., & Singer, S. 1978, *Journal of Geophysical Research: Space Physics*, 83, 75, doi: [10.1029/ja083ia01p00075](https://doi.org/10.1029/ja083ia01p00075)
- Palmerio, E., Kilpua, E. K., & Savani, N. P. 2016, *Annales Geophysicae*, doi: [10.5194/angeo-34-313-2016](https://doi.org/10.5194/angeo-34-313-2016)
- Pollock, C., Moore, T., Jacques, A., et al. 2016, *Space Science Reviews*, 199, 331, doi: [10.1007/s11214-016-0245-4](https://doi.org/10.1007/s11214-016-0245-4)
- Raghav, A., Shaikh, Z., Vemareddy, P., et al. 2023, *Solar Physics*, 298, 64, doi: [10.1007/s11207-023-02157-y](https://doi.org/10.1007/s11207-023-02157-y)
- Raghav, A. N., Choraghe, K., & Shaikh, Z. I. 2019, *Monthly Notices of the Royal Astronomical Society*, 488, 910, doi: [10.1093/mnras/stz1608](https://doi.org/10.1093/mnras/stz1608)
- Riley, P., Baker, D., Liu, Y. D., et al. 2018, *Space Science Reviews*, 214, 1, doi: [10.1007/s11214-017-0456-3](https://doi.org/10.1007/s11214-017-0456-3)
- Russell, C., & Shinde, A. 2005, *Solar Physics*, 229, 323, doi: [10.1007/s11207-005-8777-x](https://doi.org/10.1007/s11207-005-8777-x)
- Russell, C., Anderson, B., Baumjohann, W., et al. 2016, *Space Science Reviews*, 199, 189, doi: [10.1007/s11214-014-0057-3](https://doi.org/10.1007/s11214-014-0057-3)
- Shaikh, Z., Raghav, A., & Bhaskar, A. 2017, *The Astrophysical Journal*, 844, 121, doi: [10.3847/1538-4357/aa729f](https://doi.org/10.3847/1538-4357/aa729f)
- Shaikh, Z. I., Raghav, A. N., Vichare, G., Bhaskar, A., & Mishra, W. 2018, *The Astrophysical Journal*, 866, 118, doi: [10.3847/1538-4357/aae1b1](https://doi.org/10.3847/1538-4357/aae1b1)
- Smith, C. W., LâŽHeureux, J., Ness, N. F., et al. 1998, *The advanced composition explorer mission*, 613, doi: [10.1007/978-94-011-4762-0_21](https://doi.org/10.1007/978-94-011-4762-0_21)
- Sonnerup, B. U. Å., & Cahill, L. J. 1967, *Journal of Geophysical Research*, 72, 171, doi: [10.1029/jz072i001p00171](https://doi.org/10.1029/jz072i001p00171)
- St. Cyr, O., Howard, R., Sheeley Jr, N., et al. 2000, *Journal of Geophysical Research: Space Physics*, 105, 18169, doi: [10.1029/1999ja000381](https://doi.org/10.1029/1999ja000381)

- Taylor, J. B. 1974, *Physical Review Letters*, 33, 1139, doi: [10.1103/physrevlett.33.1139](https://doi.org/10.1103/physrevlett.33.1139)
- . 1986, *Reviews of Modern Physics*, 58, 741, doi: [10.1103/revmodphys.58.741](https://doi.org/10.1103/revmodphys.58.741)
- Teng, W., Su, Y., Ji, H., & Zhang, Q. 2024, *Nature Communications*, 15, 9198, doi: [10.1038/s41467-024-53538-1](https://doi.org/10.1038/s41467-024-53538-1)
- Thampi, S. V., Bhaskar, A., Mayank, P., Vaidya, B., & Venugopal, I. 2025, *The Astrophysical Journal*, 981, 76, doi: [10.3847/1538-4357/ada93c](https://doi.org/10.3847/1538-4357/ada93c)
- Tripathi, D., Chakrabarty, D., Nandi, A., et al. 2022, *Proceedings of the International Astronomical Union*, 18, 17â–27, doi: [10.1017/S1743921323001230](https://doi.org/10.1017/S1743921323001230)
- Venugopal, I., Thampi, S. V., & Bhaskar, A. 2025, *Scientific Reports*, 15, 26551, doi: [10.1038/s41598-025-08843-0](https://doi.org/10.1038/s41598-025-08843-0)
- Vichare, G., & Bagiya, M. S. 2024, *Geophysical Research Letters*, 51, e2024GL112569, doi: [10.1029/2024gl112569](https://doi.org/10.1029/2024gl112569)
- Wang, Y., Zhang, Q., Liu, J., et al. 2016, *Journal of Geophysical Research: Space Physics*, 121, 7423, doi: [10.1002/2016ja022924](https://doi.org/10.1002/2016ja022924)
- Webb, D. F., & Howard, T. A. 2012, *Living Reviews in Solar Physics*, 9, 1
- Weiler, E., Möstl, C., Davies, E. E., et al. 2025, *Space Weather*, 23, e2024SW004260, doi: [10.1029/2024sw004260](https://doi.org/10.1029/2024sw004260)
- Xie, H., Gopalswamy, N., Akiyama, S., Yashiro, S., & Makela, P. 2023, *Journal of Atmospheric and Solar-Terrestrial Physics*, 252, 106154
- Yadav, V. K., Vijaya, Y., Krishnam Prasad, B., et al. 2025, *Solar Physics*, 300, doi: [10.1007/s11207-025-02440-0](https://doi.org/10.1007/s11207-025-02440-0)
- Zhang, Y., Motoba, T., Paxton, L., & Schaefer, R. 2025, *AGU Advances*, 6, e2025AV001688, doi: [10.1029/2025AV001688](https://doi.org/10.1029/2025AV001688)